Nilsson-Kerr et al-2019-Nature Geoscience

Article *in* Nature Geoscience · April 2019

DOI: 10.1038/s41561-019-0319-5

7 authors, including:

Pallavi Anand
The Open University (UK)

Sambuddha Misra
Indian Institute of Science

Steve C Clemens
Brown University

nature geoscience

ARTICLES

https://doi.org/10.1038/s41561-019-0319-5

Role of Asian summer monsoon subsystems in the inter-hemispheric progression of deglaciation

K. Nilsson-Kerr[1]*, P. Anand[1]*, P. F. Sexton[1], M. J. Leng[2,3], S. Misra[4], S. C. Clemens[5] and S. J. Hammond[1]

The responses of Asian monsoon subsystems to both hemispheric climate forcing and external orbital forcing are currently issues of vigorous debate. The Indian summer monsoon is the dominant monsoon subsystem in terms of energy flux, constituting one of Earth's most dynamic expressions of ocean–atmosphere interactions. Yet, the Indian summer monsoon is grossly under-represented in Asian monsoon palaeoclimate records. Here, we present high-resolution records of Indian summer monsoon-induced rainfall and fluvial runoff recovered in a sediment core from the Bay of Bengal across Termination II, 139–127 thousand years ago, including coupled measurements of the oxygen isotopic composition and Mg/Ca, Mn/Ca, Nd/Ca and U/Ca ratios in surface-ocean-dwelling foraminifera. Our data reveal a millennial-scale transient strengthening of the Asian monsoon that punctuates Termination II associated with an oscillation of the bipolar seesaw. The progression of deglacial warming across Termination II emerges first in the Southern Hemisphere, then the tropics in tandem with Indian summer monsoon strengthening, and finally the Northern Hemisphere. We therefore suggest that the Indian summer monsoon was a conduit for conveying Southern Hemisphere latent heat northwards, thereby promoting subsequent Northern Hemisphere deglaciation.

Early modelling studies that attempted to evaluate the response of the boreal summer monsoon to orbital forcing identified Northern Hemisphere (NH) solar insolation (during minimum precession) as a primary driver, via its influence on land–ocean thermal contrasts[1]. Palaeoclimate records of the Indian summer monsoon (ISM) support this view, but also commonly invoke NH climate controls[2] owing to the coincidence of weak ISM intervals with North Atlantic Heinrich events[2,3]. These millennial-scale cooling events originating in the high latitudes of the NH have been linked to the ISM via atmospheric[3] and oceanic[4] teleconnections. Similarly, East Asian summer monsoon (EASM) speleothem oxygen isotope ($\delta^{18}O$) records, which are inferred to reflect both upstream depletion of $\delta^{18}O$ from tropical moisture sources and regional precipitation amount[5], have been linked to both NH solar insolation and North Atlantic forcing[6], although this interpretation has recently been questioned in light of new EASM rainfall records[7,8]. Despite this prevailing view of NH forcing of the Asian monsoon on millennial-to-orbital timescales, some observations from ISM records have pointed to additional mechanisms influencing ISM behaviour[9–11]. The nature of variance in the obliquity band and lag of ISM maxima with minimum precession suggest a component of Southern Hemisphere (SH) forcing through latent heat export[9,10]. Understanding of the ISM at timescales beyond the last glacial period mainly derives from orbital-scale records from the Arabian Sea and southern Bay of Bengal (Fig. 1a). Records from these locations have applied proxies that have been assumed to be representative of upwelling and changes in water column stratification driven by ISM winds. However, the extent to which the ISM exclusively controls these proxies remains unclear[12]. Thus, in order to enhance our understanding of the ISM, records of rainfall and runoff from the ISM's core convective region — the northern Bay of Bengal — are urgently required to isolate a primary and direct signal of ISM strength.

Here, we report new geochemical records from well-preserved planktic foraminifera at a submillennial-scale resolution (~250–500 years) spanning Termination II (TII; 139–127 thousand years ago (ka)) from International Ocean Discovery Program (IODP) Expedition 353, Site U1446 in the northern Bay of Bengal. Site U1446 is situated in the core convective region of the ISM, under the direct influence of ISM-induced rainfall and fluvial runoff received from one of the world's largest river systems (the Ganges–Brahmaputra). Figure 1b–e shows the southward propagation of the ISM-induced freshwater plume derived from the Ganges–Brahmaputra river system engulfing Site U1446 during the peak summer monsoon season. This site is thus ideally situated to capture the signal of ISM-derived rainfall, fluvial runoff and sediment delivery from the Indian subcontinent. We have produced a detailed stratigraphy for Site U1446 that is tied to the Antarctic ice core chronology (AICC2012)[13] (Methods and Supplementary Fig. 1). To evaluate changes in the surface ocean salinity response to rainfall and runoff, we combine carbonate oxygen isotope ($\delta^{18}O_c$) and Mg/Ca-derived sea-surface temperatures (SSTs) from the planktic foraminifera *Globigerinoides ruber* sensu stricto (s.s.) to reconstruct seawater $\delta^{18}O$ ($\delta^{18}O_{sw}$) (Methods and Fig. 2n (right)).

We also present Mn/Ca, Nd/Ca and U/Ca ratios (Supplementary Fig. 8) of *G. ruber* s.s. calcite in a novel application to reconstruct fluvial runoff, where high concentrations of manganese, neodymium and uranium are delivered from the continental hinterland by the ISM's vigorous hydrological and weathering regime[14–16]. This regime exerts a strong seasonal bias on the vertical and lateral distribution of dissolved 'lithogenic' elements within the Bay of Bengal[15], with a strong lithogenic signal existing in the upper 100 m of the northern Bay of Bengal as a result of high terrigenous fluxes[16]. The origin of neodymium in planktic foraminiferal calcite remains controversial, with the neodymium either reflecting the in situ seawater neodymium signal[17], conveying a mixed signal from sediments and bottom

---

[1]School of Environment, Earth and Ecosystem Sciences, Faculty of Science, Technology, Engineering and Mathematics, The Open University, Milton Keynes, UK. [2]NERC Isotope Geoscience Facilities, British Geological Survey, Nottingham, UK. [3]Centre for Environmental Geochemistry, School of Biosciences, University of Nottingham, Loughborough, UK. [4]Centre for Earth Sciences, Indian Institute of Science, Bangalore, India. [5]Earth, Environmental, and Planetary Sciences, Brown University, Providence, RI, USA. *e-mail: katrina.kerr@open.ac.uk; pallavi.anand@open.ac.uk

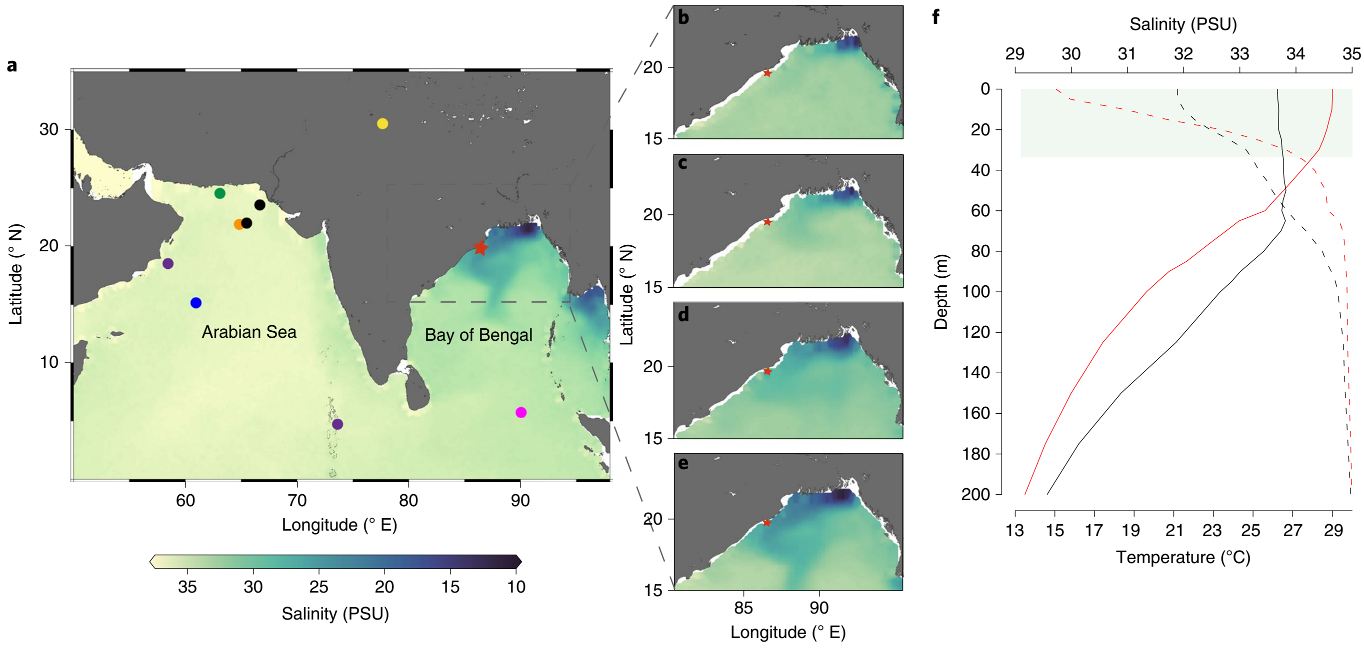

Fig. 1 | ISM-induced freshening in the Bay of Bengal. **a**, Map depicting ISM-inferred, wind-driven upwelling and stratification records (pink[42], purple[43], blue[9], orange[44], black[45] and green[10]) that extend across TII. The yellow circle indicates Bittoo Cave[2]. **b**–**e**, Average monthly sea-surface salinity during the 2017 ISM months (June, **b**; July, **c**; August, **d**; September, **e**)[46], for the region shown by a dashed box in **a**, exhibiting proliferation of fluvial input. In **a**–**e**, site U1446 is indicated by a red star. **f**, Winter (black) and summer (red) monsoon season temperature (solid lines) and salinity depth profiles (dashed lines)[47] above site U1446. The shaded bar indicates the inferred depth range of *G. ruber* s.s. PSU, practical salinity units. Figure created using Ocean Data View software (http://odv.awi.de/).

waters[18] or arising from intra-test organic matter[19]. We interpret our foraminiferal Mn/Ca, Nd/Ca and U/Ca data to reflect a primary signal of upper ocean chemistry modulated by high fluxes of lithogenic elements from high fluvial runoff, for several reasons. First, the foraminifera cleaning method we applied included a reductive cleaning step that ensures the removal of Fe–Mn coatings added onto the surface of the foraminifera test at the sediment–water interface[20]. Second, Mn/Ca correlates with Nd/Ca and U/Ca (Supplementary Fig. 7), suggesting that the concentrations of these elements are all derived from the same dominant process (that is, in this hydrographic setting, fluvial runoff). Third, the concentrations of lithogenic elements in modern seawater in the northern Bay of Bengal are much higher than in global average seawater[16] (owing to high dissolved elemental fluxes from the continent, driven by the ISM). Fourth, the observed concentrations of these elements are beyond what is typically found in planktic foraminifera[21]. We normalized Mn/Ca, Nd/Ca and U/Ca to unit variance[22] to produce a stack of *G. ruber* s.s. geochemical tracers of fluvial runoff (Fig. 2m (right) and Methods). The range of values exhibited by this runoff tracer record overlaps with the range of these same elements in modern *G. ruber* s.s., as measured from a 2005 sediment trap in the northern Bay of Bengal (red vertical bar in Fig. 2m (right)). This underscores that our *G. ruber* s.s.-based stacked record of manganese, neodymium and uranium concentrations is recording high concentrations of these elements in local seawater (derived from high runoff fluxes), rather than being a post-depositional phenomenon via diagenetic alteration of the foraminiferal calcite. Therefore, comparing *G. ruber* s.s. $\delta^{18}O_{sw}$ and *G. ruber* s.s. runoff tracers together provides a novel opportunity to reconstruct changes in both salinity and fluvial runoff sourced directly from the ISM. The application of these runoff tracers in *G. ruber* s.s. as representing ISM river fluxes is supported by elemental signatures of continental origin from discrete portable X-ray fluorescence (pXRF) measurements on bulk sediment samples that are purely diagnostic of continental detrital input from runoff (aluminium, titanium, potassium and rubidium) (Fig. 2l (right), Methods and Supplementary Fig. 9).

Our high-resolution time series of $\delta^{18}O_{sw}$, *G. ruber* s.s. runoff tracers and pXRF element stack show a similar pattern of ISM behaviour across TII, accounting for the differing intensity in the response and thresholds between surface freshening and riverine sediment fluxes[23]. The data reveal a brief intensification of the ISM from ~134–133 ka, reflected as a decrease in $\delta^{18}O_{sw}$ (Fig. 2n (right)) and an increase in *G. ruber* s.s. runoff tracers (Fig. 2m (right)) and the pXRF bulk sediment element stack (Fig. 2l (right)) late in marine isotope stage 6, before TII onset. This was immediately preceded by a ~1-kyr-duration SST warming in the Bay of Bengal (Fig. 2o (right)), suggesting that advection of SH heat across the equator provided a crucial precondition[24] for the subsequent transient strengthening of monsoonal circulation at 134 ka. Our data show that the ISM then undergoes two phases of deglacial strengthening (one at ~131–130 ka, followed by a further strengthening at ~129 ka), with the final attainment of a vigorous interglacial ISM coeval with the development of full deglaciation into the Last Interglacial (marine isotope stage 5e) (Fig. 2 (right)).

Interstadial within TII

The structures of the last two terminations—Termination I (TI) and TII—are fundamentally different (Fig. 2 and Methods). TI is punctuated by several millennial-scale events, manifested in the Bølling–Allerød (B/A) and Younger Dryas (YD), associated with fluctuations in Atlantic meridional overturning circulation[25] (Fig. 2 (left)). Such millennial-scale events have remained largely unidentified in reconstructions of TII. However, we identify a climatic event punctuating TII—evident in ISM rainfall and runoff (Fig. 2l–n (right)) at ~134–133 ka—before the timing of TII deglaciation in the NH[26]. We refer to this event as the TII Interstadial (TII IS). ISM strengthening during the TII IS was preceded by a 1 °C warming in *G. ruber* s.s.-derived SSTs at ~135 ka (Fig. 2o (right)). This warming

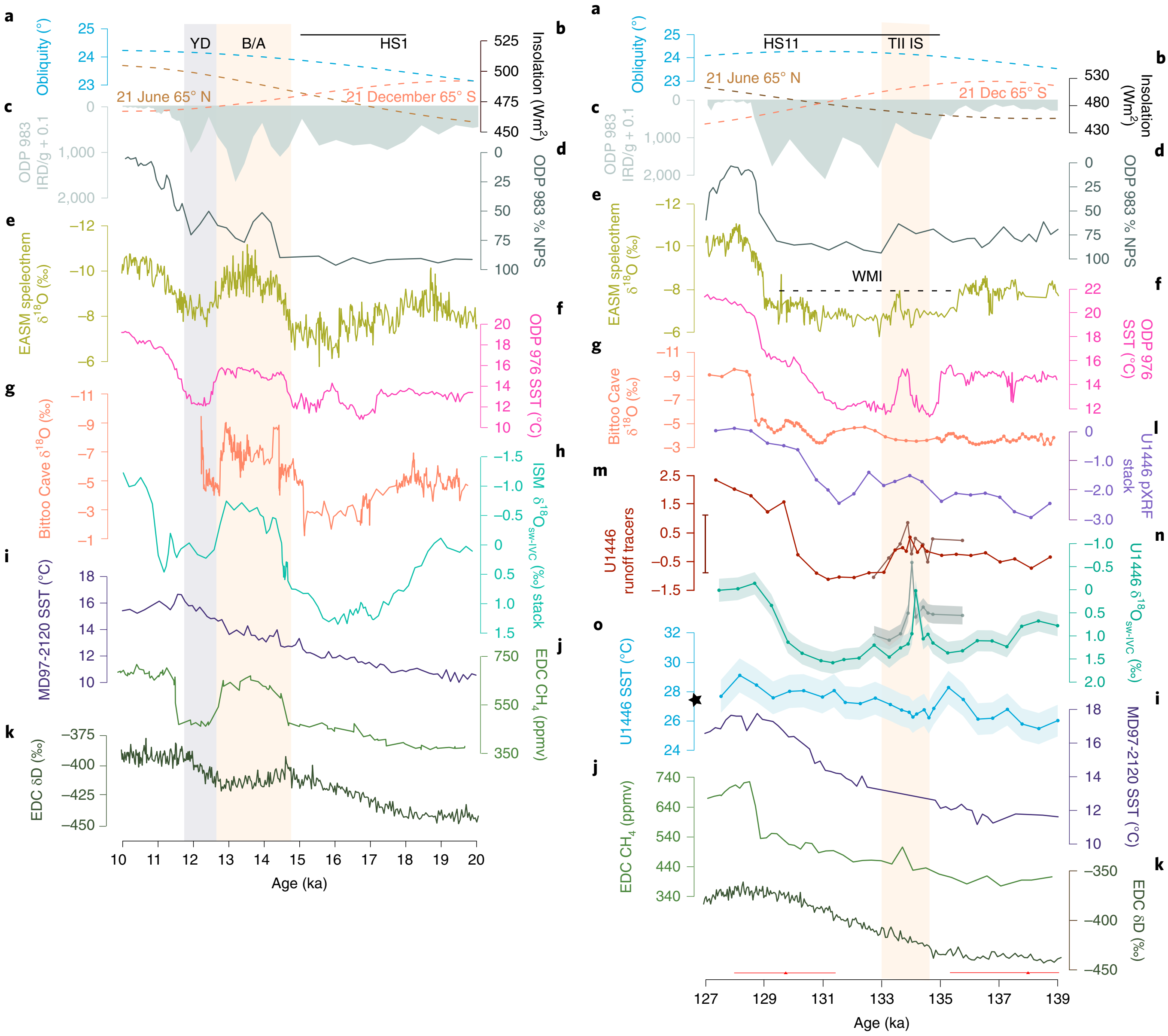

Fig. 2 | Sequences of global events. Data are shown for TI (left) and TII (right). The parameters depicted are obliquity[34] (**a**), 21 June and 21 December insolation[34] (**b**), ODP 983 (North Atlantic) Ice Rafted Debris (IRD) grains per gram[48] (**c**), ODP 983 percentage *Neogloboquadrina pachyderma sinistral* (NPS)[48] (**d**), EASM speleothem δ^{18}O (ref. [6]; **e**), ODP 976 (western Mediterranean) SST[27,29] (**f**), Bittoo Cave speleothem δ^{18}O (ref. [2]; **g**), ISM δ^{18}O$_{sw-IVC}$ stack[49–51] (normalized to unit variance, averaged and linearly interpolated onto a common age-scale, z-scores shown; **h**), Core MD97-2120 (southwest Pacific) SST[52] (**i**), EDC CH$_4$ (refs. [13,38]; **j**), EDC δD[13,53] (**k**), U1446 pXRF stack (z-scores shown) (**l**), U1446 *G. ruber* s.s. (red) and *N. dutertrei* (brown) runoff tracers (z-scores shown) (**m**; the red bar shows the modern sediment trap data range), U1446 *G. ruber* s.s. (green) and *N. dutertrei* (grey) δ^{18}O$_{sw-IVC}$ (**n**) and U1446 SST (**o**). The star represents the modern-day mean annual SST at the study site[47]. Shaded envelopes represent 1σ (Methods). Red triangles represent age-control points contained within the intervals shown, and associated AICC2012 chronology errors[13] (Methods). HS1, Heinrich Stadial 1; YD, Younger Dryas; B/A, Bølling–Allerød.

coincides with early deglaciation in the SH (Fig. 2i,k (right)), but with the establishment of cool conditions in the North Atlantic associated with Heinrich Stadial 11 (HS11) onset[27]. We infer that this SST warming in the Bay of Bengal reflects cross-equatorial heat transport in response to contemporaneous warming in the SH. These SH-derived energy fluxes, advecting northwards, lead to transient strengthening of the ISM that marks the TII IS (Fig. 2l–n (right)). We thus attribute the TII IS to a transient oscillation of the bipolar seesaw, akin to mechanisms proposed for TI[25,28]. The TII IS is also depicted in other NH records: a western Mediterranean Sea SST record[27,29] (Fig. 2f (right)) and the EASM speleothem δ^{18}O record[6,30] (Fig. 2e (right)). Further support for a cross-equatorial northward flux of SH-derived heat through a bipolar seesaw mechanism is provided by a cooling in the southeast Atlantic coeval with the TII IS, which has been attributed to a reduction in the Agulhas Leakage associated with a northward shift of the atmospheric belts towards the warmer hemisphere (the NH)[31]. The timing of TII IS is within the error of Meltwater Pulse 2B (133 ± 1 ka)[27]. Thus, it appears that TII IS may have contributed to rapid retreat of NH ice sheets and the resulting Meltwater Pulse 2B owing to heat import into the NH. The resulting enhanced freshwater fluxes into the North Atlantic[32] cause intensification of HS11 (Fig. 2c,d (right)), cooling of the NH and the end of TII IS, associated with a southward shift of the Intertropical Convergence Zone[33]. Recent work has

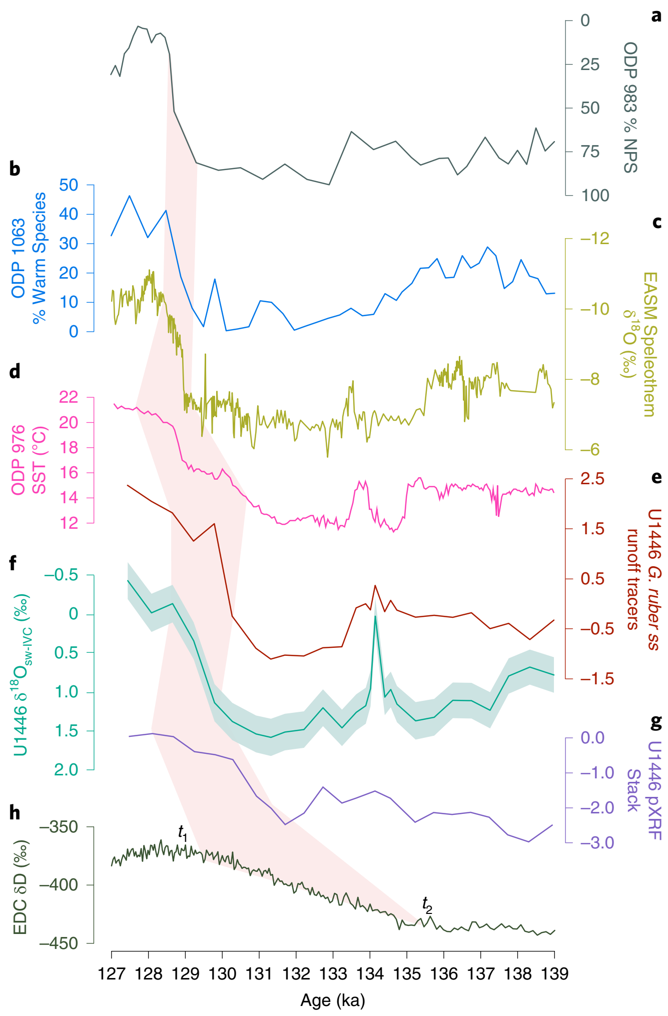

Fig. 3 | TII onset and duration. The parameters depicted are ODP 983 (North Atlantic) percentage NPS[48] on AICC2012 chronology[13] (**a**), ODP 1063 (Atlantic Ocean) percentage of warm species[54] on AICC2012 chronology[13] (**b**), EASM speleothem $\delta^{18}O$ (ref. [6]; **c**), ODP 976 (western Mediterranean Sea) SST[29] on Corchia Cave radiometrically constrained chronology[27] (**d**), U1446 *G. ruber* s.s. runoff tracer (this study; **e**), U1446 *G. ruber* s.s. $\delta^{18}O_{sw\text{-}IVC}$ (this study; **f**), U1446 pXRF stack (**g**) and EDC δD[53] on AICC2012 chronology[13] (**h**). The pink shaded area denotes t_2 (deglaciation onset) and t_1 (attainment of interglacial), as modelled using RAMPFIT[36] (Methods).

argued for a robust North Atlantic control on the EASM[6,30]. Yet, our findings for a SH origin for the transient EASM strengthening during TII IS, perhaps via the ISM, reveal that the nature of these inter-hemispheric controls on a given monsoonal subsystem is not fixed, but dynamic across different timescales.

Inter-hemispheric progression of deglaciation

The nature of deglaciation during TII is thought to be a result of orbital preconditioning; that is, an earlier maximum in SH solar insolation 10 kyr before NH solar insolation maxima, promoting earlier Antarctic warming[26] (Fig. 2b (right)). Furthermore, maximum obliquity (Fig. 2a (right)) was reached before minimum precession[34] (Fig. 2b (right)), triggering an increased inter-hemispheric temperature contrast and strengthening of the Hadley Cell in the warmer hemisphere (the SH). The colder hemisphere (the NH) is compensated by increased cross-equatorial heat transport[35]. Figure 3 shows the statistically determined timings[36] of regional deglaciation throughout TII. The combination of maximum obliquity and early deglacial SH warming (Fig. 3h) dictates that heat and moisture would have been transported to the ISM across the equator from the southern Indian Ocean. We thus conclude that SH-sourced energy fluxes (Fig. 3h) were responsible for early deglacial strengthening of the ISM at ~131–130 ka (Fig. 3e–g). Contemporaneous early deglacial warming occurred in the western Mediterranean[27,29] (Fig. 3d), and we infer that this reflects adiabatic descent from the descending limb of the Hadley Cell[37], propagating SH-sourced energy fluxes northward. This northward propagation of SH heat and moisture into higher NH latitudes was slowed by the persistence of a cold North Atlantic with HS11 (Fig. 3a,b). Subsequently, the inter-hemispheric progression of deglacial warming was propagated into the higher latitudes of the North Atlantic (Fig. 3a,b) with associated EASM strengthening (Fig. 3c). Our ISM records (Fig. 2m,n (right)) show strong covariance with the Antarctic CH_4 record (Fig. 2j (right)) during both the TII IS and broader deglaciation. This finding supports hypotheses that call for tropical wetlands as being an important global methane source during glacial–interglacial transitions, as well as hypotheses that the tropical monsoonal system plays a fundamental role in regulating concentrations of this greenhouse gas[38].

Millennial-scale phasing of Asian monsoon subsystems

Our ISM records across TII provide insights into the relationship between the two main Asian monsoon subsystems at the millennial scale. Deglacial ISM strengthening is temporally decoupled from EASM strengthening by ~1–2 kyr (Fig. 3). We infer that this lag is not associated with respective age-models, and instead ultimately reflects the time-transgressive nature of deglacial strengthening in the Asian monsoon subsystems and influence of differing forcing mechanisms triggering this strengthening. The makeup of these two monsoonal subsystems is quite different (in terms of land–ocean configurations, and atmospheric and ocean dynamics[39]); thus, it is likely that during major changes in the background climate state, the ISM and EASM exhibit such time-transgressive responses.

Our findings thus allow us to reject the hypothesis of a singular common (NH) forcing mechanism of the Asian monsoon[6]. Therefore, despite the iconic nature of the EASM speleothem records[6], our high-resolution ISM rainfall and runoff data suggest that the assumption that they are representative of the Asian monsoon as a whole needs to be reconsidered, at least on millennial time-scales. This decoupling of the ISM and EASM across TII may owe its origins to the complexities and large-scale variation in the moisture supply amalgamated in the speleothem $\delta^{18}O$ signal[8,40]. Our new records point to a greater dynamism in the mechanisms regulating Asian monsoon rainfall beyond just teleconnections to the North Atlantic[6]. This emphasises the need for more high-resolution palaeoclimate time series that are directly influenced by monsoonal rainfall, for both the EASM and ISM, to shed further light on the mechanism and feedbacks regulating monsoonal subsystems.

Our findings from TII indicate that the ISM is a key inter-hemispheric link in the transfer of heat and moisture between the warm SH and colder NH (Fig. 3). Our submillennial-scale records provide support for hypotheses that argue for an important role of the tropics[41] in conveying SH latent heat northwards into the NH, thereby promoting NH deglaciation. However, the evolution of the ISM captured in our data suggests that a fully strengthened 'interglacial' mode of the ISM cannot be attained until the NH experiences full deglacial climatic amelioration (Fig. 3). Our results highlight the need for explicit differentiation between the ISM and EASM, owing to their respective sensitivities to potentially different components of the Earth system during global climate change. Our data also reveal that inter-hemispheric climatic controls on the two primary monsoonal subsystems are dynamic across different timescales and that, during a glacial transition, these two monsoonal subsystems can be governed by different inter-hemispheric controls.

Online content

Any methods, additional references, Nature Research reporting summaries, source data, statements of data availability and associated accession codes are available at https://doi.org/10.1038/s41561-019-0319-5.

Received: 25 May 2018; Accepted: 31 January 2019;

References

1. Kutzbach, J. E. Monsoon climate of the early Holocene: climate experiment with the Earth's orbital parameters for 9000 years ago. *Science* **214**, 59–61 (1981).
2. Kathayat, G. et al. Indian monsoon variability on millennial-orbital timescales. *Sci. Rep.* **6**, 24374 (2016).
3. Deplazes, G. et al. Weakening and strengthening of the Indian monsoon during Heinrich events and Dansgaard–Oeschger oscillations. *Paleoceanogr. Paleoclimatol.* **29**, 99–114 (2014).
4. Tierney, J. E., Pausata, F. S. R. & deMenocal, P. Deglacial Indian monsoon failure and North Atlantic stadials linked by Indian Ocean surface cooling. *Nat. Geosci.* **9**, 46–50 (2015).
5. Orland, I. J. et al. Direct measurements of deglacial monsoon strength in a Chinese stalagmite. *Geology* **43**, 555–558 (2015).
6. Cheng, H. et al. The Asian monsoon over the past 640,000 years and ice age terminations. *Nature* **534**, 640–646 (2016).
7. Beck, J. W. et al. A 550,000-year record of East Asian monsoon rainfall from ^{10}Be in loess. *Science* **360**, 877–881 (2018).
8. Clemens, S. C. et al. Precession-band variance missing from East Asian monsoon runoff. *Nat. Commun.* **9**, 3364 (2018).
9. Clemens, S. C. & Prell, W. L. 350,000 year summer-monsoon multi-proxy from the Owen Ridge, Northern Arabian Sea. *Mar. Geol.* **201**, 35–51 (2003).
10. Caley, T. et al. New Arabian Sea records help decipher orbital timing of Indo-Asian monsoon. *Earth Planet. Sci. Lett.* **308**, 433–444 (2011).
11. Gebregiorgis, D. et al. Southern Hemisphere forcing of South Asian monsoon precipitation over the past ~1 million years. *Nat. Commun.* **9**, 4702 (2018).
12. Le Mézo, P., Beaufort, L., Bopp, L., Braconnot, P. & Kageyama, M. From monsoon to marine productivity in the Arabian Sea: insights from glacial and interglacial climates. *Clim. Past* **13**, 759–778 (2017).
13. Bazin, L. et al. An optimized multi-proxy, multi-site Antarctic ice and gas orbital chronology (AICC2012): 120–800 ka. *Clim. Past* **9**, 1715–1731 (2013).
14. Sarin, M. M., Krishnaswami, S., Somayajulu, B. L. K. & Moore, W. S. Chemistry of uranium, thorium, and radium isotopes in the Ganga-Brahmaputra river system: weathering processes and fluxes into the Bay of Bengal. *Geochim. Cosmochim. Acta* **54**, 1387–1396 (1990).
15. Singh, S. P. et al. Spatial distribution of dissolved neodymium and $\varepsilon_{\mathrm{Nd}}$ in the Bay of Bengal: role of particulate matter and mixing of water mass. *Geochim. Cosmochim. Acta* **94**, 38–56 (2012).
16. Yu, Z. et al. Seasonal variations in dissolved neodymium isotope composition in the Bay of Bengal. *Earth Planet. Sci. Lett.* **479**, 310–321 (2017).
17. Vance, D. & Burton, K. Neodymium isotopes in planktonic foraminifera: a record of the response of continental weathering and ocean circulation rates to climate change. *Earth Planet. Sci. Lett.* **173**, 365–379 (1999).
18. Pomiès, C., Davies, G. R. & Conan, S. M.-H. Neodymium in modern foraminifera from the Indian Ocean: implications for the use of foraminiferal Nd isotope compositions in paleo-oceanography. *Earth Planet. Sci. Lett.* **203**, 1031–1045 (2002).
19. Martínez-Botí, M. A., Vance, D. & Mortyn, P. G. Nd/Ca ratios in plankton-towed and core top foraminifera: confirmation of the water column acquisition of Nd. *Geochem. Geophys. Geosyst.* **10**, Q08018 (2009).
20. Boyle, E. A. & Keigwin, L. D. Comparison of Atlantic and Pacific paleochemical records for the last 215,000 years: changes in deep ocean circulation and chemical inventories. *Earth Planet. Sci. Lett.* **76**, 135–150 (1985).
21. Russell, A. N., Emerson, S., Nelson, B. K., Erez, J. & Lea, D. W. Uranium in foraminiferal calcite as recorder of seawater uranium concentrations. *Geochim. Cosmochim. Acta* **58**, 671–681 (1994).
22. Abdi, H. & Williams, L. J. in *Encyclopoedia of Research Design* 935–938 (ed. Salkind, N.) (Sage, Thousand Oaks, 2010).
23. Dearing, J. A. & Jones, R. T. Coupling temporal and spatial dimensions of global sediment flux through lake and marine sediment records. *Glob. Planet. Change* **39**, 147–168 (2003).
24. McCreary, J. P., Kundu, P. K. & Molinari, R. L. A numerical investigation of dynamics, thermodynamics and mixed-layer processes in the Indian Ocean. *Prog. Oceanogr.* **31**, 181–244 (1993).
25. Barker, S. et al. Interhemispheric Atlantic seesaw response during the last deglaciation. *Nature* **457**, 1097–1101 (2009).
26. Broecker, W. S. & Henderson, G. M. The sequence of events surrounding Termination II and their implications for the cause of glacial-interglacial CO_2 changes. *Paleoceanogr. Paleoclimatol.* **13**, 352–364 (1998).
27. Marino, G. et al. Bipolar seesaw control on last interglacial sea level. *Nature* **522**, 197–201 (2015).
28. Knorr, G. & Lohmann, G. Rapid transitions in the Atlantic thermohaline circulation triggered by global warming and meltwater during the last deglaciation. *Geochem. Geophys. Geosyst.* **8**, Q12006 (2007).
29. Martrat, B., Jimenez-Amat, P., Zahn, R. & Grimalt, J. O. Similarities and dissimilarities between the last two deglaciations and interglaciations in the North Atlantic region. *Quat. Sci. Rev.* **99**, 122–134 (2014).
30. Cheng, H. et al. Ice age terminations. *Science* **326**, 248–252 (2009).
31. Scussolini, P., Marino, G., Brummer, G.-J. & Peeters, F. J. C. Saline Indian Ocean waters invaded the South Atlantic thermocline during glacial termination II. *Geology* **43**, 139–142 (2015).
32. Carlson, A. E. & Winsor, K. Northern Hemisphere ice-sheet responses to past climate warming. *Nat. Geosci.* **5**, 607–613 (2012).
33. Broccoli, A. J., Dahl, K. A. & Stouffer, R. J. Response of the ITCZ to Northern Hemisphere cooling. *Geophys. Res. Lett.* **33**, L01702 (2006).
34. Laskar, J. et al. A long-term numerical solution for the insolation quantities of the Earth. *Astron. Astrophys.* **428**, 261–285 (2004).
35. Mantis, D. F. et al. The response of large-scale circulation to obliquity-induced changes in meridional heating gradients. *J. Clim.* **27**, 5504–5516 (2014).
36. Mudelsee, M. Ramp function regression: a tool for quantifying climate transitions. *Comput. Geosci.* **26**, 293–307 (2000).
37. Rodwell, M. J. & Hoskins, B. J. Subtropical anticyclones and summer monsoons. *J. Clim.* **14**, 3192–3211 (2001).
38. Loulergue, L. et al. Orbital and millennial-scale features of atmospheric CH_4 over the past 800,000 years. *Nature* **453**, 383–386 (2008).
39. Wang, B., Clemens, S. C. & Liu, P. Contrasting the Indian and East Asian monsoons: implications on geologic timescales. *Mar. Geol.* **201**, 5–21 (2003).
40. Caley, T., Roche, D. M. & Renssen, H. Orbital Asian summer monsoon dynamics revealed using an isotope-enabled global climate model. *Nat. Commun.* **5**, 5371 (2014).
41. Rodgers, K. B. et al. A tropical mechanism for Northern Hemisphere deglaciation. *Geochem. Geophys. Geosyst.* **4**, 1046 (2003).
42. Bolton, C. T. et al. A 500,000 year record of Indian summer monsoon dynamics recorded by eastern equatorial Indian Ocean upper water-column structure. *Quat. Sci. Rev.* **77**, 167–180 (2013).
43. Budziak, D. et al. Late Quaternary insolation forcing on total organic carbon and C_{37} alkenone variations in the Arabian Sea. *Paleoceanogr. Paleoclimatol.* **15**, 307–321 (2000).
44. Ziegler, M. et al. Precession phasing offset between Indian summer monsoon and Arabian Sea productivity linked to changes in Atlantic overturning circulation. *Paleoceanogr. Paleoclimatol.* **25**, PA3213 (2010).
45. Reichart, G.-J., Lourens, L. J. & Zachariasse, W. J. Temporal variability in the northern Arabian Sea oxygen minimum zone (OMZ) during the last 225,000 years. *Paleoceanogr. Paleoclimatol.* **13**, 607–621 (1998).
46. Meissner, T. & Wentz, F. J. *Remote Sensing Systems SMAP Ocean Surface Salinities (Level 3 Monthly)* v.3.0 (Remote Sensing Systems, 2018); www.remss.com/missions/smap
47. Boyer, T. P. et al. *World Ocean Database 2013* (National Environmental, Satellite, Data, and Information Service, 2013).
48. Barker, S. et al. Icebergs not the trigger for North Atlantic cold events. *Nature* **520**, 333–336 (2015).
49. Kudrass, H. R., Hofmann, A., Doose, H., Emeis, K. & Erlenkeuser, H. Modulation and amplification of climatic changes in the Northern Hemisphere by the Indian summer monsoon during the past 80 k.y. *Geology* **29**, 63–66 (2001).
50. Rashid, H., Flower, B. P., Poore, R. Z. & Quinn, T. M. A ~25 ka Indian Ocean monsoon variability record from the Andaman Sea. *Quat. Sci. Rev.* **26**, 2586–2597 (2007).
51. Saraswat, R., Lea, D. W., Nigam, R., Mackensen, A. & Naik, D. K. Deglaciation in the tropical Indian Ocean driven by interplay between the regional monsoon and global teleconnections. *Earth Planet. Sci. Lett.* **375**, 166–175 (2013).
52. Pahnke, K. & Sachs, J. P. Sea surface temperatures of southern midlatitudes 0–160 kyr B.P. *Paleoceanogr. Paleoclimatol.* **21**, PA2003 (2006).
53. Jouzel, J. et al. Orbital and millennial Antarctic climate variability over the past 800,000 years. *Science* **317**, 793–795 (2007).
54. Deaney, E. L., Barker, S. & van de Flierdt, T. Timing and nature of AMOC recovery across Termination 2 and magnitude of deglacial CO_2 change. *Nat. Commun.* **8**, 14595 (2017).

Acknowledgements

We thank P. Webb for help setting up the pXRF analysis, H. Sloane for help with the stable isotope analysis, and P. D. Naidu for providing the 2005 NBBT-05-S sediment traps. P.A. would like to express gratitude to Ministry of Earth Sciences, Government of India, for drilling permissions for Expedition 353 and UK-IODP for funding support. P.A. would also like to thank Expedition 353 shipboard scientists for their efforts and Kochi Core Repository, Japan, for sampling support. SMAP salinity data are produced by Remote Sensing Systems and sponsored by the NASA Ocean Salinity Science Team. P.A. and K.N.-K. acknowledge funding through a NERC PhD grant (NE/L002493/1) associated with the CENTA Doctoral Training Partnership. Samples were provided by the IODP. Stable isotope analysis of planktic foraminifera was funded by NIGFSC grant IP-1649-1116 to P.A.

Author contributions

P.A. conceived the research idea and further developed it with K.N.-K. K.N.-K. processed samples, picked foraminifera, and conducted foraminifera cleaning and trace element analysis under guidance from P.A. and S.M. M.J.L. oversaw the stable isotope analysis. S.J.H. helped with trace element analysis. S.C.C. produced benthic oxygen isotope data for age model development. K.N.-K., P.A. and P.F.S. discussed data interpretation and wrote the manuscript. All authors contributed to the final text.

Competing interests

The authors declare no competing interests.

Additional information

Supplementary information is available for this paper at https://doi.org/10.1038/s41561-019-0319-5.

Reprints and permissions information is available at www.nature.com/reprints.

Correspondence and requests for materials should be addressed to K.N. or P.A.

Publisher's note: Springer Nature remains neutral with regard to jurisdictional claims in published maps and institutional affiliations.

Methods

Site U1446 (19° 5.02′ N, 85° 44′ E) was drilled during IODP Expedition 353 and located at a depth of 1,430 m below sea level in the Mahanadi Basin[55]. The Bay of Bengal represents the core convective region of the ISM due to the thermodynamic structure of the water column resulting in positive ocean–atmosphere feedbacks favouring high SSTs (>28 °C) allowing convection to be sustained during the summer monsoon months of June through to September[56]. The ISM exerts a strong seasonal signature of surface water freshening and stratification within the Bay of Bengal due to a net surface water exchange of $184 \times 10^{10}\,\mathrm{m}^3$ during the ISM months[57]. ISM-induced river runoff generates a north–south salinity gradient; the northern Bay of Bengal undergoes a reduction in salinity of 9% during this period[58].

Age model. The much expanded nature of the sediment sequence at Site U1446 (~25 cm kyr^{-1}) and consequent high fidelity of our palaeoclimatic records significantly reduce the error of the duration of events and the rates of change inferred from our records[59]. Using AnalySeries[60], we graphically correlated benthic foraminifera (*Uvigerina* species and *Cibicidoides wuellerstorfi*) δ^{18}O (S.C.C., unpublished data) to benthic δ^{18}O from the south Pacific core PS75/059-2 (ref. [61]) (Supplementary Fig. 1a). This itself is tied to the AICC2012 chronology[13] by exploiting the age–depth relationship from the PS75/059-2 iron dust flux record[62], which has been tuned to the European Project for Ice Coring in Antarctica (EPICA) DOME C (EDC) Antarctic ice core[62,63] (Supplementary Fig. 2). Tuning to AICC2012 was chosen, rather than the absolute dated EASM speleothem record, to allow for independent assessment of the lead–lag relationship between the ISM and EASM. We infer that our records are not biased to the high latitudes of the SH by our tuning strategy due to synchronicity existing between the Chinese Loess magnetic susceptibility record with EDC Antarctic ice core dust fluxes[63]. To ascertain our confidence in our age model, we further tied U1446 benthic δ^{18}O to Ocean Drilling Program (ODP) Leg 117, Site 1146 benthic δ^{18}O, which has been transferred to the speleothem chronology[64]. We present site U1446 benthic δ^{18}O on three different age models (AICC2012 (ref. [13]), RC2011 (ref. [64]) and LR04 (ref. [65]); Supplementary Fig. 1c) to confirm the lead of U1446 ISM records over the EASM across TII regardless of chronology (Supplementary Fig. 3).

We used Bchron[66]—a Bayesian probability model—to model the 95% uncertainty envelope between tie points with the AICC2012 chronology error (modelled as Gaussian distribution) of EDC Antarctic ice core at those points[13] (Supplementary Fig. 1b).

All datasets used to assess relative lead and lag relationships are on a consistent age-model—that of AICC2012 (ref. [13])—or absolute radiometrically constrained chronology[2,6,27] (see original references for details).

Foraminiferal stable isotope and trace element analysis. The planktic foraminifera *G. ruber* s.s., was identified using the taxonomic description in ref. [67]. Between 6 and 30 individuals were picked from the 250–355 µm size-fraction and gently crushed before analysis. Oxygen isotope analyses were performed at the British Geological Survey, Natural Environment Research Council Isotope Geoscience Facilities, Keyworth using an Isoprime dual inlet mass spectrometer with a Multiprep device. The reproducibility of oxygen isotope measurements is ±0.05‰ (1σ) based on replicate measurements of carbonate standards. All data are reported in the usual delta notation (δ^{18}O) in ‰ on the Vienna PeeDee Belemnite (VPDB) scale.

For trace element analysis, samples were cleaned using a modification of the method described in ref. [20] and reversal of the oxidative and reductive steps[68]. Due to the proximal setting of Site U1446, an extended clay removal step was essential to ensure removal of any fine clays that may bias magnesium content in carbonate samples. Samples were initially rinsed with repeated Milli-Q and methanol rinses, with ultrasonification of 40 seconds between each rinse. Samples were then inspected under a microscope, and any discoloured fragments and fragments with pyrite or silicate particles were removed. Subsequently, samples were subjected to a reductive and 10% oxidative step to ensure the removal of any coatings and organics. Samples were then polished using a weak (0.001 M) HNO_3 leaching step and dissolved (0.075 M HNO_3) on the day of analysis. Samples were analysed at the Open University using an Agilent Technologies Triple-Quadrupole ICP-MS. Contaminant ratios (Al/Ca and Fe/Ca) were monitored to assess any clay and organic contaminations (Supplementary Fig. 4).

Estimating temperature and $\delta^{18}\mathrm{O}_{\mathrm{sw}}$. The addition of a reductive step during foraminiferal trace element cleaning has been shown to reduce Mg/Ca values[69]. Following ref. [70], we apply a correction for a 10% reduction in Mg/Ca associated with the reductive method due to the chosen temperature calibration being based on analysis using only the oxidative step[71]. The Mg/Ca temperature calibration used was accordingly adjusted:

$\mathrm{Mg/Ca} = 0.38(\pm 0.02)\,\exp((0.09 \pm 0.003) \times T)$[71]

Adjusted $\mathrm{Mg/Ca} = 0.342\,\exp(0.09T)$

An ice-volume correction (IVC) was applied to the calcite $\delta^{18}\mathrm{O}_{\mathrm{c}}$ following the Red Sea level curve (95% probability maximum)[72], with a conversion factor δ^{18}O enrichment of 0.008‰ per metre of sea level lowering applied[73], where t represents a specific point in time:

$\delta^{18}\mathrm{O}_{\mathrm{IVC}}(t) = \delta^{18}\mathrm{O}(t) + (\mathrm{RSL}(t) \times 0.008)$

The temperature estimates derived from Mg/Ca and the measured calcite $\delta^{18}\mathrm{O}_{\mathrm{c}}$ of planktic foraminifera allow for the derivation of seawater $\delta^{18}\mathrm{O}_{\mathrm{sw}}$:

$T(°\mathrm{C}) = 14.9(\pm 0.1) - 4.8(\pm 0.08) \times (\delta^{18}\mathrm{O}_{\mathrm{c}} - \delta^{18}\mathrm{O}_{\mathrm{sw}}) - 0.27‰$[74]

$\delta^{18}\mathrm{O}_{\mathrm{sw}}$ has been shown to correlate strongly with salinity in the northern Bay of Bengal. Factors controlling this relationship include precipitation, river runoff and evaporation; thus, during the summer monsoon months, precipitation and runoff exceed evaporation, promoting a low $\delta^{18}\mathrm{O}_{\mathrm{sw}}$–salinity slope[75,76]. However, we do not convert U1446 $\delta^{18}\mathrm{O}_{\mathrm{sw}}$ to salinity using modern-day calculated regressions due to the observation of significant spatiotemporal variations and uncertainties in assumptions associated with extending these relationships into the past[75]. Furthermore, recent work has indicated the potential control salinity exerts on magnesium incorporation in foraminiferal calcite[77]. Low salinity during the warmer ISM season may potentially dampen our reconstructed SSTs based on Mg/Ca relative to actual SSTs; however, there would be a limited overall effect on the reconstructed $\delta^{18}\mathrm{O}_{\mathrm{sw}}$.

Neogloboquadrina dutertrei is typically inferred to represent thermocline conditions (~70–120 m) accompanying the deep chlorophyll maximum[78,79]. However, across the TII IS, *N. dutertrei* shows more depleted oxygen isotope composition of seawater values, corrected for ice volume ($\delta^{18}\mathrm{O}_{\mathrm{sw\text{-}IVC}}$), than surface-dwelling *G. ruber* s.s. (Fig. 2n (right)). We infer that this is associated with the unique hydrographic conditions that Site U1446 experiences, and that *N. dutertrei* occupies a shallower depth (in the freshwater lens of the upper water column) than is typically inferred. Additionally, available Mg/Ca calibrations based on upper thermocline habitat, and therefore a narrower temperature range, underestimate the temperature values for *N. dutertrei*, thus resulting in more depleted $\delta^{18}\mathrm{O}_{\mathrm{sw\text{-}IVC}}$ values as the calcite δ^{18}O values are more enriched than for *G. ruber* s.s. (Supplementary Fig. 5). During the TII IS, *G. ruber* s.s. and *N. dutertrei* $\delta^{18}\mathrm{O}_{\mathrm{sw\text{-}IVC}}$ are decoupled by ~100 years (Fig. 2n (right)), highlighting the vertical flux of ISM-induced freshening.

Error propagation of the temperature and $\delta^{18}\mathrm{O}_{\mathrm{sw}}$ estimates was calculated using the following equations[80], where Mg/Ca standard deviation is 0.029 mmol mol^{-1} and $\delta^{18}\mathrm{O}_{\mathrm{c}}$ is 0.05‰ based on repeated analysis of internal standards. The error propagation is based on assumptions of no covariance among a, b, T and $\delta^{18}\mathrm{O}_{\mathrm{c}}$[80]. For error propagation associated with temperatures derived from Mg/Ca:

$$\sigma_T^2 = \left(\frac{T}{\mathrm{a}}\sigma_{\mathrm{a}}\right)^2 + \left(\frac{T}{\mathrm{b}}\sigma_{\mathrm{b}}\right)^2 + \left(\frac{T}{\mathrm{Mg/Ca}}\sigma_{\mathrm{Mg/Ca}}\right)^2$$

where:

a = 0.342 ± 0.02 (ref. [71])
b = 0.09 ± 0.003 (ref. [71])

$$\frac{T}{\mathrm{a}} = -\frac{1}{\mathrm{a}^2}\ln\left(\frac{\mathrm{Mg/Ca}}{\mathrm{b}}\right)$$

$$\frac{T}{\mathrm{b}} = -\frac{1}{\mathrm{ab}}$$

$$\frac{T}{\mathrm{Mg/Ca}} = \frac{1}{\mathrm{a}} \times \frac{1}{\mathrm{Mg/Ca}}$$

For calculation of errors associated with the estimation of the oxygen isotope composition of seawater:

$$\sigma^2_{\delta^{18}\mathrm{O}_{\mathrm{sw}}} = \left(\frac{\delta^{18}\mathrm{O}_{\mathrm{sw}}}{T}\sigma_T\right)^2 + \left(\frac{\delta^{18}\mathrm{O}_{\mathrm{sw}}}{\mathrm{a}}\sigma_{\mathrm{a}}\right)^2 + \left(\frac{\delta^{18}\mathrm{O}_{\mathrm{sw}}}{\mathrm{b}}\sigma_{\mathrm{b}}\right)^2 + \left(\frac{\delta^{18}\mathrm{O}_{\mathrm{sw}}}{\delta^{18}\mathrm{O}_{\mathrm{c}}}\sigma_{\delta^{18}\mathrm{O}_{\mathrm{c}}}\right)^2$$

where:

a = 14.9 ± 0.1 (ref. [74])
b = −4.8 ± 0.08 (ref. [74])

$$\frac{\delta^{18}\mathrm{O}_{\mathrm{sw}}}{T} = -\frac{1}{\mathrm{b}}$$

$$\frac{\delta^{18}\mathrm{O}_{\mathrm{sw}}}{\mathrm{a}} = \frac{1}{\mathrm{b}}$$

$$\frac{\delta^{18}\mathrm{O}_{\mathrm{sw}}}{\mathrm{b}} = \frac{T}{\mathrm{b}^2} - \frac{\mathrm{a}}{\mathrm{b}^2}$$

$$\frac{\delta^{18}\mathrm{O}_{\mathrm{sw}}}{\delta^{18}\mathrm{O}_{\mathrm{c}}} = 1$$

To further constrain errors associated with calculating SST and $\delta^{18}\mathrm{O}_{\mathrm{sw}}$, we used Paleo-Seawater Uncertainty Solver (PSUSolver)[81]. PSUSolver models uncertainties associated with age model, calibrations, and analytical and sea level estimate errors, by performing bootstrap Monte Carlo simulations[81]. Accounting for AICC2012 age-model errors[13], we input an average age-model error of 2 ka and analytical errors for Mg/Ca and $\delta^{18}O_c$ of 0.029 mmol mol^{-1} and 0.05‰, respectively, for PSUSolver to probabilistically constrain the median estimate and confidence intervals for SST and $\delta^{18}O_{sw}$ (Supplementary Fig. 6a). To assess the influence age-model error exerts on U1446 SST and $\delta^{18}O_{sw}$, we also input age model errors of 1 ka (Supplementary Fig. 6b) and 0 ka (Supplementary Fig. 6c). This indicates that age-model errors exert the strongest influence on PSUSolver SST and $\delta^{18}O_{sw}$. An average age-model error of 2 ka renders the TII IS inconspicuous. However, we have confidence in our original U1446 SST and $\delta^{18}O_{sw}$ interpretations despite the associated errors with the AICC2012 chronology owing to TII IS having been resolved in other independently dated records (Fig. 2 (right)) and the coherence of U1446 $\delta^{18}O_{sw}$ with deglacial warming in western Mediterranean Sea SST records from ODP Site 976 (ref. [29]) (Fig. 3), which has a radiometrically constrained age model[27].

Interpreting Mn/Ca, Nd/Ca and U/Ca as river runoff proxies. Mn/Ca ratios measured in foraminifera are typically used as an indicator of contamination of foraminifer calcite from authigenic manganese-rich oxide coatings on the foraminifer shell. Our Mn/Ca data display no correlation with Mg/Ca (pearson correlation coefficient, $r^2 = 0.0894$), strongly arguing against the presence of manganese-rich oxide coatings on our foraminifera that would bias our Mg/Ca-derived SSTs. The foraminifera cleaning method applied in this study included a reductive cleaning step, ensuring the removal of Fe–Mn coatings added to the carbonate tests at the sediment-water interface[20,69]. Mn/Ca correlates with Nd/Ca and U/Ca (Supplementary Fig. 7), reinforcing evidence that these elements are delivered to our study site via fluvial runoff and can thus be used as runoff proxies in this proximal setting. High fluvial fluxes in the Bay of Bengal reflect the monsoon region's vigorous hydrological and concomitant weathering regime. This is expressed by the vast quantities of material discharged via the rivers; the Ganges–Brahmaputra system alone contributes 1.06×10^9 tonnes of sediment annually[82]. Such a unique hydrographic setting allows high concentrations of dissolved lithogenic elements (manganese, neodymium and uranium) to be precipitated (either as authigenic or biogenic carbonate phases) on mixing with seawater. The observed concentrations of these elements at Site U1446 are well beyond the concentrations that are typically found in planktic foraminifera[21]. Similarly, elevated levels of Mn/Ca, Nd/Ca and U/Ca ratios have been found in planktic foraminifera from Ceara Rise ODP Site 926, which receives Amazon fluvial fluxes[83,84]. Furthermore, we generated trace element data for *G. ruber* s.s. from Northern Bay of Bengal Trap-2005-Surface (NBBT-05-S) sediment traps from the northern Bay of Bengal. The range of values exhibited by this runoff tracer record (manganese, neodymium and uranium) overlaps with the range found in the NBBT-05-S sediment trap data (Fig. 2m (right)). Thus, we interpret Mn/Ca, Nd/Ca and U/Ca ratios in *G. ruber* s.s. (Supplementary Fig. 8) as a proxy for fluvial runoff at marginal sites, and suggest that they could be further ground-truthed for application in other marginal marine settings. Owing to the similarity between Mn/Ca, Nd/Ca and U/Ca, we normalize using the standard deviation[22]:

$$/\mathrm{Ca}(t)_{\mathrm{norm}} = \frac{/\mathrm{Ca}(t) - \overline{/\mathrm{Ca}}}{\sigma(/\mathrm{Ca})}$$

where:

$/\mathrm{Ca}(t)$ (for example, Mn/Ca) represents the trace-element-to-Ca ratio at a given time.

$\overline{/\mathrm{Ca}}$ represents the mean of all of the trace-element-to-Ca ratios (for example, Mn/Ca) across the study interval.

$\sigma(/\mathrm{Ca})$ represents the standard deviation of the trace-element-to-Ca ratio across the study interval.

Subsequently, we average these values ($/\mathrm{Ca}(t)_{\mathrm{norm}}$) for each of the tracers to produce a factor representing *G. ruber* s.s. runoff tracers. Furthermore, there is a similar signature among these tracers with the data gained from pXRF (Supplementary Fig. 9).

Discrete pXRF analysis. Analysis of major and minor elements was performed using a Niton XL3t900 pXRF. Before analysis, 5 g of material was weighed, dried in an oven at 40 °C and subsequently homogenized into a fine powder through the use of a pestle and mortar. The powdered material was transferred into 7 ml vials, sealed tightly with non-polyvinyl chloride cling film and placed flush over the aperture of the X-ray emitter (M. Saker-Clark, personal communication). Calibration for each element of interest was performed by analysis of geochemical in-house and reference powdered rock standards with known concentrations. A set of internal and reference standards were run every 10th sample for quality control (Supplementary Table 1). Bulk sediment elemental geochemistry was controlled by detrital (that is, terrigenous input via river runoff) and authigenic processes. Therefore, to reconstruct ISM-derived river runoff, a selection of inferred terrigenous-derived elements were selected to represent increased fluvial runoff and detrital input to the site; titanium, potassium, aluminium and rubidium (Supplementary Fig. 9). These elements were combined by normalizing to the unit variance (described in the above section for *G. ruber* s.s. runoff tracers) to produce a factor of pXRF runoff element variations[22], due to them showing strong correlation with each other (Supplementary Fig. 10). To clarify the inconsistency in the elements chosen to represent fluvial runoff between the pXRF element stack and *G. ruber* s.s. tracers: (1) uranium concentrations in discrete U1446 samples were below the detection limit and neodymium was not measured; and (2) manganese concentrations in ocean sediments were complicated by redox processes; therefore, this was not a suitable candidate for representing the detrital phase in bulk sediment elemental profiles. We infer that, due to increased terrigenous supply during a strengthened ISM, reduced bottom water conditions are established, resulting in manganese reduction and dissolution into pore waters due to the increased solubility of reduced manganese (Mn^{2+})[85–88]. In contrast, during times of weaker ISM and reduced terrigenous supply, aerobic conditions promote the formation of solid-phase manganese oxyhydroxides and thus manganese concentrations increase in the bulk sediment (Supplementary Fig. 9)[85–88]. This reasoning is coherent with conditions found in the Cariaco Basin, which is proximal to high terrigenous fluxes via river runoff[89].

Detection of TII change points. To empirically assess deglaciation onset during TII, we employed the RAMPFIT[36] algorithm. RAMPFIT segments the data into three parts using a weighted least-squares regression and brute force to find two breakpoints denoted as t_1 and t_2 (ref. [36]). RAMPFIT was used to estimate the following: deglaciation onset (t_1) and duration (t_2) in the EASM speleothem $\delta^{18}O$ record[6], ODP 976 western Mediterranean Sea SST[27,29], ODP 1063 percentage of warm species[54], ODP 983 percentage *Neogloboquadrina pachyderma sinistral* (NPS)[48], EDC δD[53] and U1446 $\delta^{18}O_{sw}$, *G. ruber* s.s. runoff tracers and pXRF stack (Fig. 3). These records were chosen to identify the proliferation of deglaciation across the NH having propagated from the SH. Some 400 iterations of wild bootstrap with seed a generator number of 400 were used to determine the uncertainties (Supplementary Table. 2).

Comparison of TII with TI. The same methods described above were employed to characterize deglaciation across TI (Supplementary Fig. 10). Our results for TII demonstrate the sequence of deglaciation having been driven from the SH, a lagged NH response and the ISM contributing to the inter-hemispheric transfer of heat and moisture. Furthermore, we highlight the out-of-phase behaviour between the EASM and ISM (Fig. 3). However, this is in contrast with the sequence of events across TI in which the ISM appears to be in-phase with the EASM and other NH climate records (Supplementary Fig. 11). Our results from TII thus exemplify the heterogeneity between TI and TII that draws on previous work in which orbital preconditioning is regarded as the driver in dictating the internal climate feedback response[90,91]. Furthermore, the behaviour of the ISM during TII may be a result of the anomalous orbital conditions that stray from classic Milankovitch theory[92]. The early rise in NH solar insolation during TI is thought to have initiated deglaciation, with rapid NH ice-sheet retreat occurring from ~19–20 ka[93], resulting in Atlantic meridional overturning circulation shutdown and subsequent warming in the SH[94]. This is in contrast with TII, where the earlier rise in SH summer insolation occurs 10 ka before NH solar insolation increase[26,95]. Based on the opposing hemispheric controls on the ISM during TI and TII, we postulate that the ISM is not hemispherically biased but is governed by inter-hemispheric climate controls compared with the predominantly NH-forced EASM[6].

Data availability

Data generated from this study (IODP Expedition 353; Site U1446) are available via the National Geoscience Data Centre (https://doi.org/10.5285/061d77af-a805-4cf0-b969-0b8f042fae74). Antarctic EDC ice core records presented on AICC2012 chronology are available from https://doi.pangaea.de/10.1594/PANGAEA.824883 and https://doi.pangaea.de/10.1594/PANGAEA.824891. The EASM composite speleothem $\delta^{18}O$ record is available from https://www.ncdc.noaa.gov/paleo-search/study/20450. The Bittoo Cave speleothem $\delta^{18}O$ record is available from https://www.ncdc.noaa.gov/paleo-search/study/20449. ODP 983 and 1063 data are available as a supplementary dataset associated with ref. [54]. ODP 976 western Mediterranean Sea SST data on Corchia radiometrically constrained chronology are available as a supplementary dataset associated with ref. [27]. Data on benthic $\delta^{18}O$ levels of sediment core PS75/059-2 are available at https://doi.org/10.1594/PANGAEA.833422. Data from sediment core PS75/059-2 on AICC2012 chronology are available at https://doi.org/10.1594/PANGAEA.826580.

References

55. Clemens, S. C. et al. In *Proc. International Ocean Discovery Program* 353 (International Ocean Discovery Program, 2016).
56. Shenoi, S. S. C., Shankar, D. & Shetye, S. R. Differences in heat budgets of the near-surface Arabian Sea and Bay of Bengal: implications for the summer monsoon. *J. Geophys. Res. Oceans* **107**, 3052 (2002).
57. Varkey, M. J., Murty, V. S. N. & Suryanarayana, A. Physical oceanography of the Bay of Bengal and Andaman Sea. *Oceanogr. Mar. Biol. Annu. Rev.* **34**, 1–70 (1996).
58. Zweng, M. M. J. R. et al. *World Ocean Atlas 2013. Volume 2: Salinity* (eds Levitus, S. & Mishonov, A.) (National Environmental Satellite, Data, and Information Service, 2013).

59. Kemp, D. B. & Sexton, P. F. Time-scale uncertainty of abrupt events in the geologic record arising from unsteady sedimentation. *Geology* **42**, 891–894 (2014).
60. Paillaird, D., Labeyrie, L. & Yiou, P. Macintosh Program performs time-series analysis. *EOS Trans.* **77**, 379 (1996).
61. Ullermann, J. et al. Pacific–Atlantic circumpolar deep water coupling during the last 500 ka. *Paleoceanogr. Paleoclimatol.* **31**, 639–650 (2016).
62. Lamy, F. et al. Increased dust deposition in the Pacific Southern Ocean during glacial periods. *Science* **343**, 403–407 (2014).
63. Lambert, F. et al. Dust–climate couplings over the past 800,000 years from the EPICA Dome C ice core. *Nature* **452**, 616–619 (2008).
64. Caballero-Gill, R. P., Clemens, S. C. & Prell, W. L. Direct correlation of Chinese speleothem δ^{18}O and South China Sea planktonic δ^{18}O: transferring a speleothem chronology to the benthic marine chronology. *Paleoceanogr. Paleoclimatol.* **27**, PA2203 (2012).
65. Lisiecki, L. E. & Raymo, M. E. A Pliocene-Pleistocene stack of 57 globally distributed δ^{18}O records. *Paleoceanogr. Paleoclimatol.* **20**, PA1003 (2005).
66. Haslett, J. & Parnell, A. A simple monotone process with application to radiocarbon-dated depth chronologies. *J. R. Stat. Soc. Ser. C* **57**, 339–418 (2008).
67. Wang, L. Isotopic signals in two morphotypes of *Globigerinoides ruber* (white) from the South China Sea: implications for monsoon climate change during the last glacial cycle. *Palaeogeogr. Palaeoclimatol. Palaeoecol.* **161**, 381–394 (2000).
68. Rosenthal, Y., Boyle, E. A. & Labeyrie, L. Last Glacial Maximum paleochemistry and deepwater circulation in the Southern Ocean: evidence from foraminiferal cadmium. *Paleoceanogr. Paleoclimatol.* **12**, 787–796 (1997).
69. Barker, S., Greaves, M. & Elderfield, H. A study of cleaning procedures used for foraminiferal Mg/Ca paleothermometry. *Geochem. Geophys. Geosyst.* **4**, 8407 (2003).
70. Gibbons, F. T. et al. Deglacial δ^{18}O and hydrologic variability in the tropical Pacific and Indian oceans. *Earth Planet. Sci. Lett.* **387**, 240–251 (2014).
71. Anand, P., Elderfield, H. & Conte, M. H. Calibration of Mg/Ca thermometry in planktonic foraminifera from a sediment trap time series. *Paleoceanogr. Paleoclimatol.* **18**, 1050 (2003).
72. Grant, K. M. et al. Rapid coupling between ice volume and polar temperature over the past 150,000 years. *Nature* **491**, 744–747 (2012).
73. Adkins, J. F., McIntyre, K. & Schrag, D. P. The salinity, temperature, and δ^{18}O of the glacial deep ocean. *Science* **298**, 1769–1773 (2002).
74. Bemis, B. E., Spero, H. J., Bijma, J. & Lea, D. W. Reevaluation of the oxygen isotopic composition of planktonic foraminifera: experimental results and revised paleotemperature equations. *Paleoceanogr. Paleoclimatol.* **13**, 150–160 (1998).
75. Singh, A., Jani, R. A. & Ramesh, R. Spatiotemporal variations of the δ^{18}O–salinity relation in the northern Indian Ocean. *Deep Sea. Res. Pt I* **57**, 1422–1431 (2010).
76. Delaygue, G. et al. Oxygen isotope/salinity relationship in the northern Indian Ocean. *J. Geophys. Res.* **106**, 4565–4574 (2001).
77. Gray, W. R. et al. The effects of temperature, salinity, and the carbonate system on Mg/Ca in *Globigerinoides ruber* (white): a global sediment trap calibration. *Earth Planet. Sci. Lett.* **482**, 607–620 (2018).
78. Ravelo, A. C. & Fairbanks, R. G. Oxygen isotopic composition of multiple species of planktonic Foraminifera: recorders of the modern photic zone temperature gradient. *Paleoceanogr. Paleoclimatol.* **7**, 815–831 (1992).
79. Mohtadi, M. et al. Reconstructing the thermal structure of the upper ocean: insights from planktic foraminifera shell chemistry and alkenones in modern sediments of the tropical eastern Indian Ocean. *Paleoceanogr. Paleoclimatol.* **26**, PA3219 (2011).
80. Bevington, P. R. & Robinson, K. D. *Data Reduction and Error Analysis for the Physical Sciences* 3rd edn (McGraw-Hill, New York, 2003).
81. Thirumalai, K., Quinn, T. M. & Marino, G. Constraining past seawater δ^{18}O and temperature records developed from foraminiferal geochemistry. *Paleoceanogr. Paleoclimatol.* **31**, 1409–1422 (2016).
82. Milliman, J. D. & Syvitski, J. P. M. Geomorphic/tectonic control of sediment discharge to the ocean: the importance of small mountainous rivers. *J. Geol.* **100**, 525–544 (1992).
83. Stewart, J. A., James, R. H., Anand, P. & Wilson, P. A. Silicate weathering and carbon cycle controls on the Oligocene–Miocene glaciation. *Paleoceanogr. Paleoclimatol.* **32**, 1070–1085 (2017).
84. Stewart, J. A., Gutjahr, M., James, R. H., Anand, P. & Wilson, P. A. Influence of the Amazon River on the Nd isotope composition of deep water in the western equatorial Atlantic during the Oligocene–Miocene transition. *Earth Planet. Sci. Lett.* **454**, 132–141 (2016).
85. Calvert, S. E. & Price, N. B. Diffusion and reaction profiles of dissolved manganese in the pore waters of marine sediments. *Earth Planet. Sci. Lett.* **16**, 245–249 (1972).
86. Thomson, J., Higgs, N. C., Croudace, I. W., Colley, S. & Hydes, D. J. Redox zonation of elements at an oxic/post-oxic boundary in deep-sea sediments. *Geochim. Cosmochim. Acta.* **57**, 579–595 (1993).
87. Calvert, S. E. & Pedersen, T. F. Geochemistry of recent oxic and anoxic marine sediments: implications for the geological record. *Mar. Geol.* **113**, 67–88 (1993).
88. Burdige, D. J. The biogeochemistry of manganese and iron reduction in marine sediments. *Earth Sci. Rev.* **35**, 249–284 (1993).
89. Yarincik, K. M., Murray, R. W., Lyons, T. W., Peterson, L. C. & Haug, G. H. Oxygenation history of bottom waters in the Cariaco Basin, Venezuela, over the past 578,000 years: results from redox-sensitive metals (Mo, V, Mn, and Fe). *Paleoceanogr. Paleoclimatol.* **15**, 593–604 (2000).
90. Carlson, A. E. Why there was not a Younger Dryas-like event during the Penultimate Deglaciation. *Quat. Sci. Rev.* **27**, 882–887 (2008).
91. Alley, R. B., Brook, E. J. & Anandakrishnan, S. A northern lead in the orbital band: north–south phasing of Ice-Age events. *Quat. Sci. Rev.* **21**, 431–441 (2002).
92. Hays, J. D., Imbrie, K. & Shackleton, N. J. Variations in the Earth's orbit: pacemaker of the ice ages. *Science* **194**, 1121–1132 (1974).
93. Clark, P. U. et al. The Last Glacial Maximum. *Science* **325**, 710–714 (2009).
94. He, F. et al. Northern Hemisphere forcing of Southern Hemisphere climate during the last deglaciation. *Nature* **494**, 81–85 (2013).
95. Masson-Delmotte, V. et al. Abrupt change of Antarctic moisture origin at the end of Termination II. *Proc. Natl Acad. Sci. USA* **107**, 12091–12094 (2010).